WILEY-VCH

Symmetrical Molecular Topology Enables Ultrathin Solid Polymer Electrolytes for Stable Lithium-Metal Batteries

Kai Chen, Anjun Hu, Wei Yang, Yuanjian Li, Zhi Wei Seh, Fei Li*, Jianping Long*, Shimou Chen**

K. Chen, Dr. A. Hu, W. Yang, Prof. Dr. J. Long
College of Materials and Chemistry & Chemical Engineering (College of Lithium Resources and Lithium Battery Industry), Chengdu University of Technology, Chengdu 610059, China.
E-mail: anjunhu@cdut.edu.cn; longjianping@cdut.cn

Prof. Dr. Shimou Chen
State Key Laboratory of Chemical Resource Engineering, Beijing Key Laboratory of Electrochemical Process and Technology of Materials, Beijing University of Chemical Technology, Beijing, 10029, P. R. China.
E-mail: chensm@mail.buct.edu.cn

Dr. A. Hu
Key Laboratory of Sichuan Province for Lithium Resources Comprehensive Utilization and New Lithium Based Materials for Advanced Battery Technology, Chengdu 610059, China.

Dr. Y. Li, Prof. Dr. Z. W. Seh
Institute of Materials Research and Engineering (IMRE) Agency for Science, Technology and Research (A*STAR) 2 Fusionopolis Way, Innovis #08-03, Singapore 138634, Singapore.

Prof. Dr. Fei Li
School of Materials and Energy, University of Electronic Science and Technology of China, Chengdu 610054, China.
E-mail: feili@uestc.edu.cn

Abstract

Solid polymer electrolytes (SPEs) have emerged as promising candidates for lithium-metal batteries owing to their advantages in safety, flexibility, and processability. However, ultrathin SPEs (<10 μm) still face challenges in practical applications, including structural inhomogeneity, sluggish ion transport, and lithium dendrite penetration. This study breaks through the conventional paradigm of compositional modulation and proposes a symmetrical molecular topology design strategy based on 2,2-Bis(4-allyloxy-3,5-dibromophenyl)propane (BADBP) polymerization network. The diallyloxy symmetric structure of BADBP bridges and constructs a 3D crosslinked network, effectively repairing the pore defects in the poly(vinylidene fluoride-co-hexafluoropropylene) matrix, achieving an ultrathin thickness of 6 μm with high mechanical robustness and uniform ion channels. The bromophenyl groups in BADBP reduce the crystallinity of the matrix via steric hindrance effects, while the high bond energy of C−Br bonds endows the electrolyte with exceptional thermal stability. Moreover, bromine atoms electrostatically anchor $TFSI^-$ anions, promoting lithium salt dissociation and forming an LiF/LiBr-rich interphase layer. As a result, the modified Li||$LiNi_{0.8}Co_{0.1}Mn_{0.1}O_2$ cells demonstrate stable cycling at both room temperature and 60°C, along with 5C fast-charging capability. The pouch cell further passes nail penetration and high-temperature safety tests. This work establishes a design paradigm for designing high-performance ultrathin solid-state electrolytes in lithium-metal batteries.

Keywords: Solid-state batteries; Lithium-metal batteries; Polymer electrolytes; Molecular topology; Crosslinked network

Introduction

Solid polymer electrolytes (SPEs) have gained prominence as essential components in high-energy-density solid-state lithium-metal batteries (LMB), owing to their inherent safety, adaptability, and superior compatibility with lithium-metal anodes.[1–5] However, commercialization necessitates ultrathin SPEs (<10 μm) to reduce internal resistance and cell weight,[6,7] thereby enhancing overall energy density.[8–10] The development of ultrathin SPEs currently faces multiple bottlenecks. First, polymer matrices (e.g., poly(vinylidene fluoride-co-hexafluoropropylene), PH) tend to form porous defects during film formation, causing discontinuous Li^+ transport pathways and inhomogeneous current density distribution that triggers dendrite growth, compromising battery safety.[11] Second, the limited amorphous phase fraction restricts ionic mobility, resulting in generally low room-temperature ionic conductivity (<0.1 mS cm^{-1}) that fails to meet high-rate charging/discharging requirements.[12] Moreover, conventional SPEs lack sufficient mechanical strength to effectively suppress dendrite penetration. [13] More critically, thermal softening or decomposition of polymer chains at elevated temperatures accelerates interfacial failure, leading to rapid cycling life deterioration.[14] These issues collectively hinder the practical implementation of ultrathin SPEs.

To address these challenges, conventional modification strategies primarily focus on performance enhancement through compositional optimization. For instance, incorporating inorganic fillers (e.g., Al_2O_3 nanoparticles, LLZO ceramics) can markedly enhance the mechanical robustness and thermal resistance properties of SPEs.[15] However, inhomogeneous filler dispersion causes aggregation, disrupting electrolyte structural homogeneity and consequently impeding Li^+ transport. While plasticizers increase Li^+ mobility by expanding amorphous regions, randomly distributed pores

fail to establish percolation networks and adversely impacts both the structural integrity and thermal resistance characteristics of SPEs. [16] Furthermore, single-ion conductors (e.g., lithium polystyrene sulfonate) do enhance Li^+ transference numbers via covalently fixed anions, but often require complex chemical modifications that challenge large-scale production while maintaining performance consistency. [17] Particularly for ultrathin SPE systems, reduced thickness amplifies these negative impacts, highlighting the inherent limitations of traditional composition-based strategies.[18,19]

Recently, *in situ* crosslinked networks have garnered significant attention due to their capability to tune polymer microstructures.[20] Nevertheless, existing ultraviolet curing/thermal-initiated crosslinking approaches, while improving ionic conductivity and dendrite resistance, still exhibit notable shortcomings. On one hand, conventional crosslinked polymers (e.g., linear polyethylene oxide, PEO) typically enhance mechanical strength through increased crosslinking density, but their topological disorder limits amorphous phase content, reducing ionic conductivity.[21] On the other hand, common crosslinked networks may still develop micron-scale pores (>1 μm) during film formation due to uneven solvent evaporation, where porous structures induce localized Li^+ flux concentration and consequent dendrite growth.[22] Additionally, ordinary crosslinked networks undergo chain segment softening above 60°C, causing abrupt declines in mechanical strength and thermal stability. Therefore, reconstructing the geometric configuration of *in situ* crosslinked SPEs through molecular topology design is crucial for achieving structure-property synergy. [23-24]

This work proposes a symmetrical molecular topology design strategy, where 2,2-bis(4-allyloxy-3,5-dibromophenyl)propane (BADBP) is employed as the functional additive unit for PH/LiTFSI

(donated as PHL) electrolytes to construct a three-dimensional crosslinked ultrathin (6 μm) SPE (donated as BADBP-PHL). Through molecular-scale structural engineering, this design simultaneously resolve porous defects, low ionic conductivity, and compromised thermal stability in conventional ultrathin SPEs (**Figure** 1). First, the diallyloxy symmetric framework of BADBP forms an interpenetrating network with PHL through radical polymerization, effectively filling the porous defects of the matrix and constructing continuous and uniform Li^+ transport channels, thereby increasing the room-temperature ionic conductivity to 0.35 mS cm^{-1}, which represents significant improvement compared to conventional PHL electrolytes (<0.1 mS cm^{-1}). Second, the bromophenyl groups of BADBP suppress the regular arrangement of PVDF chains through steric hindrance effects, increasing the proportion of amorphous regions and providing more free volume for Li^+ migration. Meanwhile, the high bond energy of C−Br bonds (~312.27 J mol^{-1}) [25] endows the network with excellent thermal stability, ensuring structural integrity at elevated temperatures. Furthermore, the strong electronegativity of bromine atoms electrostatically anchors $TFSI^-$ anions, promoting the dissociation of LiTFSI. Concurrently, the *in situ* film-forming effect induced by bromine groups facilitates the generation of a robust solid electrolyte interphase (SEI) rich in LiF/LiBr, enhancing interfacial stability. Based on this symmetrical molecular topology design, the Li||Li symmetric cell with 6 μm BADBP-PHL demonstrates stable cycling for 2000 hours at 0.1 mA cm^{-2}. The modified Li||$LiNi_{0.8}Co_{0.1}Mn_{0.1}O_2$ (NCM811) cell retains 82.4% of its capacity after 230 cycles at room temperature and 96% after 150 cycles at 60°C, while withstanding 5C fast charging. As practical validation, the fabricated pouch cells demonstrate stable cycling and can withstand severe mechanical

and thermal abuse, confirming their high safety characteristics. This study provides both theoretical breakthroughs and a materials innovation paradigm for the practical application of ultrathin SPEs.

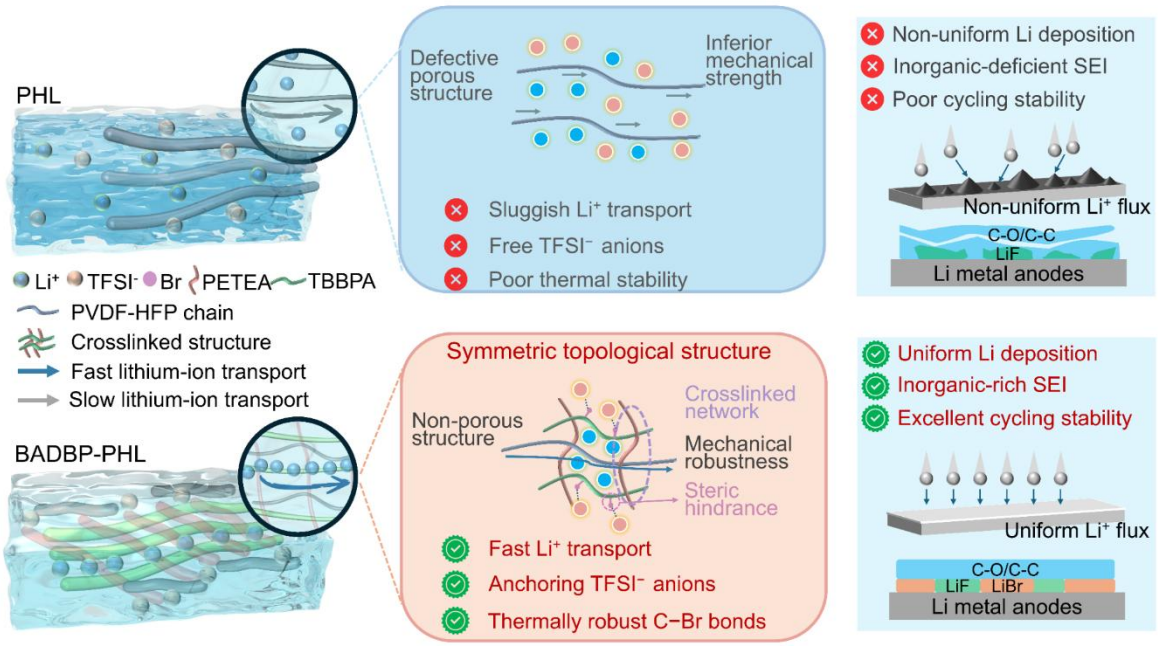

Figure 1. Conceptual schematic diagram of the symmetric topological structure of BADBP-PHL.

Results and discussion

Construction and multiscale characterization of BADBP-PHL

The BADBP-PHL solid electrolyte membrane was fabricated via a standard solution-casting technique. PH was dissolved in a N,N-dimethylformamide solvent containing LiTFSI to form PHL, followed by sequential addition of the symmetrical molecules BADBP and pentaerythritol tetraacrylate (PETEA). Upon introducing the initiator (azobisisobutyronitrile), crosslinking polymerization was carried out at 120°C, yielding the final BADBP-PHL electrolyte film. To characterize the formation of the symmetrical molecular topological network, Fourier-transform infrared (FTIR) spectroscopy analysis was conducted. As depicted in **Figure** 2a, the disappearance

of characteristic C=C double bond peaks at 1640 cm^{-1} (PETEA) and 1660 cm^{-1} (BADBP), along with the retention of the C−Br bond peak at 570 cm^{-1}, confirm the successful crosslinking polymerization of BADBP and PETEA via the diallyloxy symmetric structure.[26,27] This structural homogeneity directly enhances the tensile strength of BADBP-PHL from 7.5 MPa to 13.4 MPa (Figure 2b). Elemental distribution analysis of the BADBP-PHL film was performed using scanning electron microscopy (SEM) and energy-dispersive X-ray spectroscopy (EDS). As shown in Figure 2c, the EDS mapping results demonstrate a homogeneous distribution of Br elements throughout the film. High-resolution SEM (Figures 2d and e) reveals that the symmetrical topological network effectively eliminated porous defects in the PHL film, forming a dense structure with a surface roughness of only 23 nm (Figure S1). Moreover, the introduction of the crosslinked topological network endows the BADBP-PHL film with a Young's modulus of 3.51 GPa (Figure 2f), achieving an optimal combination of ultrathin thickness (6 μm) and high mechanical strength.

The symmetrical molecular topology demonstrates distinct advantages in thermal stability. As illustrated in Figure S2, BADBP-PHL maintains structural integrity at 160°C, while polypropylene separators and PHL undergo polycondensation at 110°C, attributable to the structural stability of the symmetrical crosslinked network and the high bond energy of C−Br. Furthermore, flame resistance tests (Figure 2g) visually demonstrate superior flame-retardant properties. Raman analysis (Figure S3) of the dense char layer formed after combustion reveals that BADBP-PHL exhibits a lower intensity ratio of D-band to G-band (I_D/I_G) compared to PHL, indicating that the incorporation of the symmetrical crosslinked network facilitates the formation of a more stable char layer during combustion, thereby enhancing structural integrity and thermal stability.[28] Thermogravimetric

analysis (TGA) (Figure 2h) confirms that BADBP-PHL possesses a higher thermal decomposition temperature, with consistently lower mass loss than PHL throughout the heating process.[29] This study demonstrates that the symmetrical topological structure formed by crosslinking BADBP with PETEA not only reinforces mechanical properties but also significantly improves thermal stability.

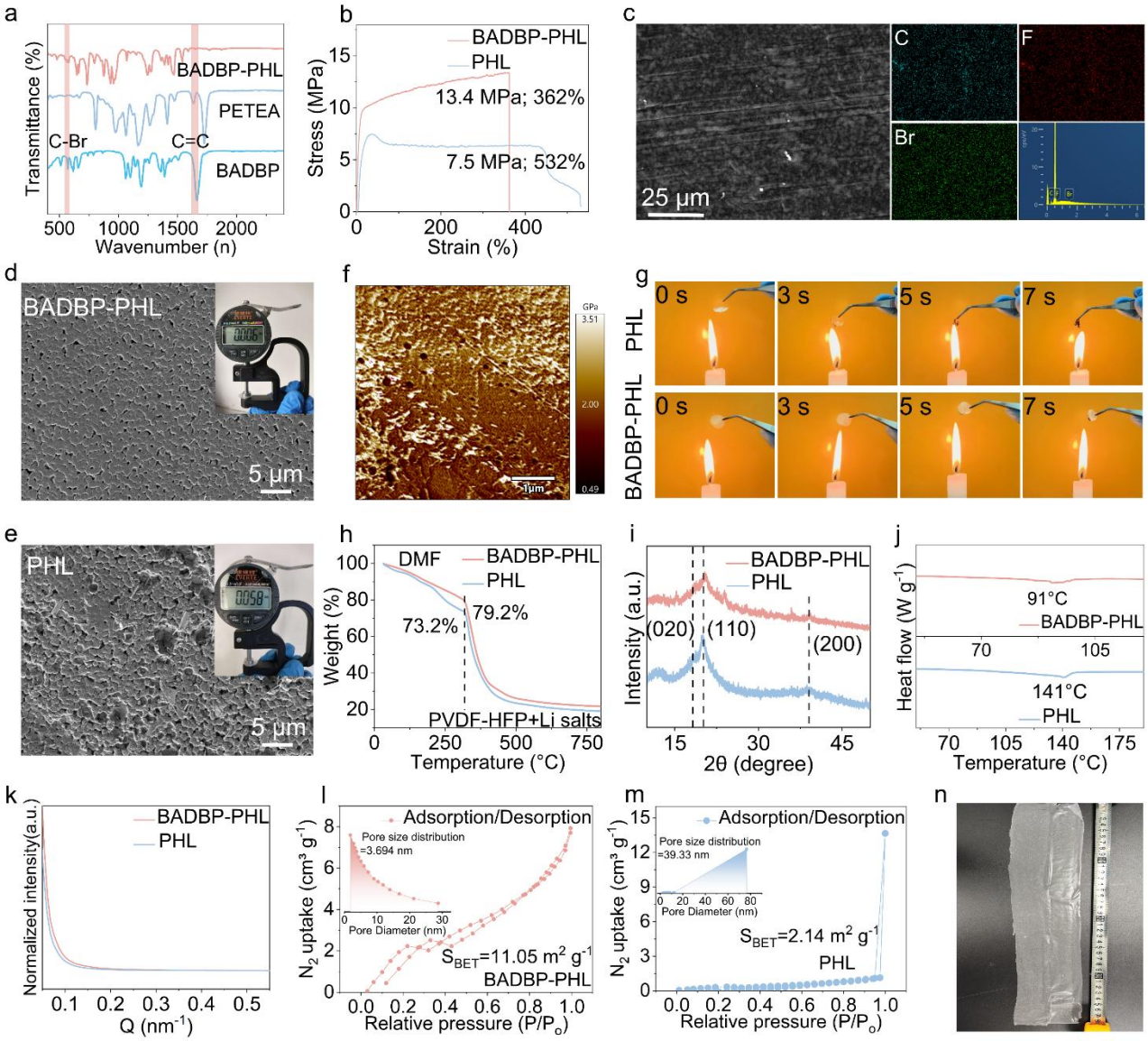

Figure 2. Structural and physicochemical characterization of BADBP-PHL. (a) Infrared spectra of BADBP-PHL, PETEA and BADBP. (b) Stress-strain curves of BADBP-PHL and PHL. (c) EDS of BADBP-PHL. SEM and thickness of (d) BADBP-PHL and (e) PHL. (f) Young's modulus of BADBP-PHL. (g) Ignition test of PHL and BADBP-PHL. (h) TGA curves of BADBP-PHL and PHL. (i) XRD patterns of BADBP-PHL and PHL. (j) DSC curves of BADBP-PHL and PHL. (k) 2D-SAXS patterns of BADBP-PHL and PHL.

Nitrogen adsorption-desorption isotherms and specific surface area of (l) BADBP-PHL and (m) PHL (inset showing the pore size distribution). (n) Large-area fabrication demonstration of BADBP-PHL.

X-ray diffraction (XRD) analysis (Figure 2i) demonstrates a significant reduction in the intensity of α-phase PH characteristic peaks. This observation, combined with differential scanning calorimetry (DSC) results showing a decrease in glass transition temperature (T_g) from 141°C to 91°C (Figure 2j), confirms that the symmetrical steric hindrance effect of bromophenyl groups effectively suppresses the regular arrangement of polymer chains.[30,31] Notably, small-angle X-ray scattering (SAXS) (Figure 2k) verifies that this modification preserves the intrinsic microstructure of PH while achieving performance enhancement through topological interconnection.[32] Brunauer-Emmett-Teller (BET) surface area analysis (Figures 2l and m) further reveals that the symmetrical topological structure reduces the average pore size from 39.33 nm to 3.694 nm. This reduction indicates successful repair of porous defects in conventional PHL membranes through polymer structure incorporation, which facilitates ion transport homogenization and mechanical property improvement.[33] Furthermore, this symmetrical molecular design endows BADBP-PHL with exceptional mechanical flexibility (Figures 2n and S4), enabling it to withstand repeated folding without fracture. The combination of rigidity and flexibility provides crucial advantages for practical applications of SPE.

Ion transport mechanism regulated by BADBP-PHL

Multiscale characterization reveals the critical role of symmetrical molecular topology in regulating ion transport. Molecular dynamics (MD) simulations (**Figure** 3a) present equilibrium snapshots of PHL and BADBP-PHL, demonstrating that the crosslinked network structure in BADBP-PHL leads

to a more compact morphology. Density functional theory (DFT) calculations (Figure 3b) indicate that the binding energy of Li^+ with BADBP-PHL is higher than that with PHL, suggesting enhanced Li^+ transfer capability in BADBP-PHL. Similarly, BADBP-PHL exhibits stronger binding energy with $TFSI^-$ anions, confirming its superior ability to immobilize anions. As shown in Figure 3c, the Li^+ diffusion coefficient in BADBP-PHL (0.022 $Å^2$/ps) is higher than that in PHL (0.016 $Å^2$/ps), which is primarily attributed to the optimized interaction between functional groups in the polymer matrix and Li^+.

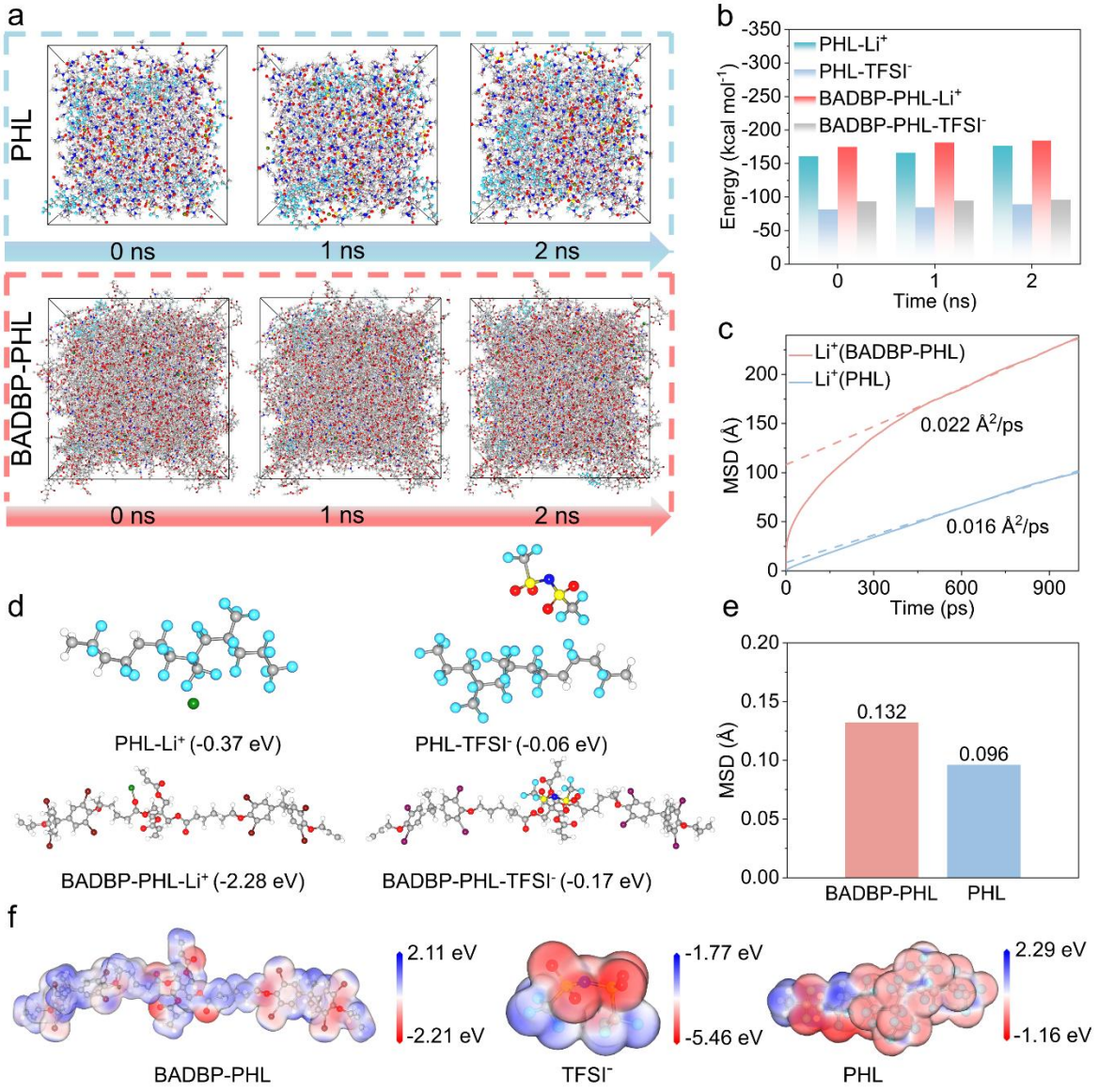

Figure 3. Computational simulations and theoretical analysis of ion transport mechanisms. (a) MD simulations of the aggregation structures of PHL and BADBP-PHL. (b) Calculated binding energies of Li^+ or $TFSI^-$ with PHL or BADBP-PHL. (c) Li^+ diffusion coefficients of PHL and BADBP-PHL. (d) Adsorption energies of Li^+ and $TFSI^-$ on PHL or BADBP-PHL. (e) MSD of Li^+ in BADBP-PHL and PHL. (f) Electrostatic potential of BADBP-PHL, $TFSI^-$ and PHL.

To elucidate the ion regulation mechanism of individual components, we calculated the adsorption energies of Li^+ and $TFSI^-$ with each constituent. As depicted in Figure 3d, the crosslinked system exhibits significantly higher adsorption energy for $TFSI^-$ (−0.17 eV) compared to PH (−0.06

eV), while demonstrating even stronger Li^+ adsorption (−2.28 eV *vs.* −0.37 eV). These results indicate that the designed structure not only preserves the Li^+ transport capability of PH but also establishes additional fast-transport channels. This potent adsorption effect, on the one hand, immobilizes $TFSI^-$ to promote lithium salt dissociation; on the other hand, it guides efficient Li^+ migration along the crosslinked topological framework, substantially enhancing ionic conductivity. Mean square displacement (MSD) analysis (Figure 3e) confirms higher Li^+ flux in BADBP-PHL. Electrostatic potential mapping (Figure 3f) reveals that low-electrostati potential sites of C−Br/C−O groups and the strong electronegativity of bromine atoms effectively anchor $TFSI^-$, facilitating salt dissociation while suppressing interfacial degradation caused by anion migration. Theoretical calculations collectively demonstrate that the symmetrical topology optimizes Li^+ transport pathways through selective $TFSI^-$ immobilization, thereby improving ion migration efficiency.

The theoretical predictions were experimentally verified using solid-state nuclear magnetic resonance (SSNMR) and Raman spectra. As shown in **Figure** 4a, the downfield shift of the Li^+ peak in BADBP-PHL signifies a significantly increased proportion of free Li^+ ions.[34] Figures 4b, c reveal that the $TFSI^-$−coordinated Li^+ ratio ($TFSI^-$−Li^+ coordination) in PHL (34.1%) is higher than that in BADBP-PHL (15.3%). This distinctive ion-state transformation results in an enhanced Li^+ transference number (t_{Li^+} = 0.65 for BADBP-PHL *vs.* 0.44 for PHL, Figure 4d) and increased exchange current density (i_0, Figure 4e). Furthermore, the electrochemical stability window of BADBP-PHL expands to 4.5 V (compared to 3.6 V for PHL, Figure 4f), demonstrating the interfacial stability advantages of the symmetrical molecular design. Temperature-dependent ionic conductivity measurements (Figure 4g) show that the symmetrical topology enables BADBP-PHL to maintain

superior conductivity across the entire temperature range. And the room-temperature ionic conductivity of BADBP-PHL is 0.35 mS cm^{-1}, superior to that of PHL (0.27 mS cm^{-1}). Arrhenius analysis (Figure 4h) confirms a lower activation energy (E_a = 0.12 eV) for BADBP-PHL compared to PHL (0.20 eV), indicating more favorable transport energy barriers.

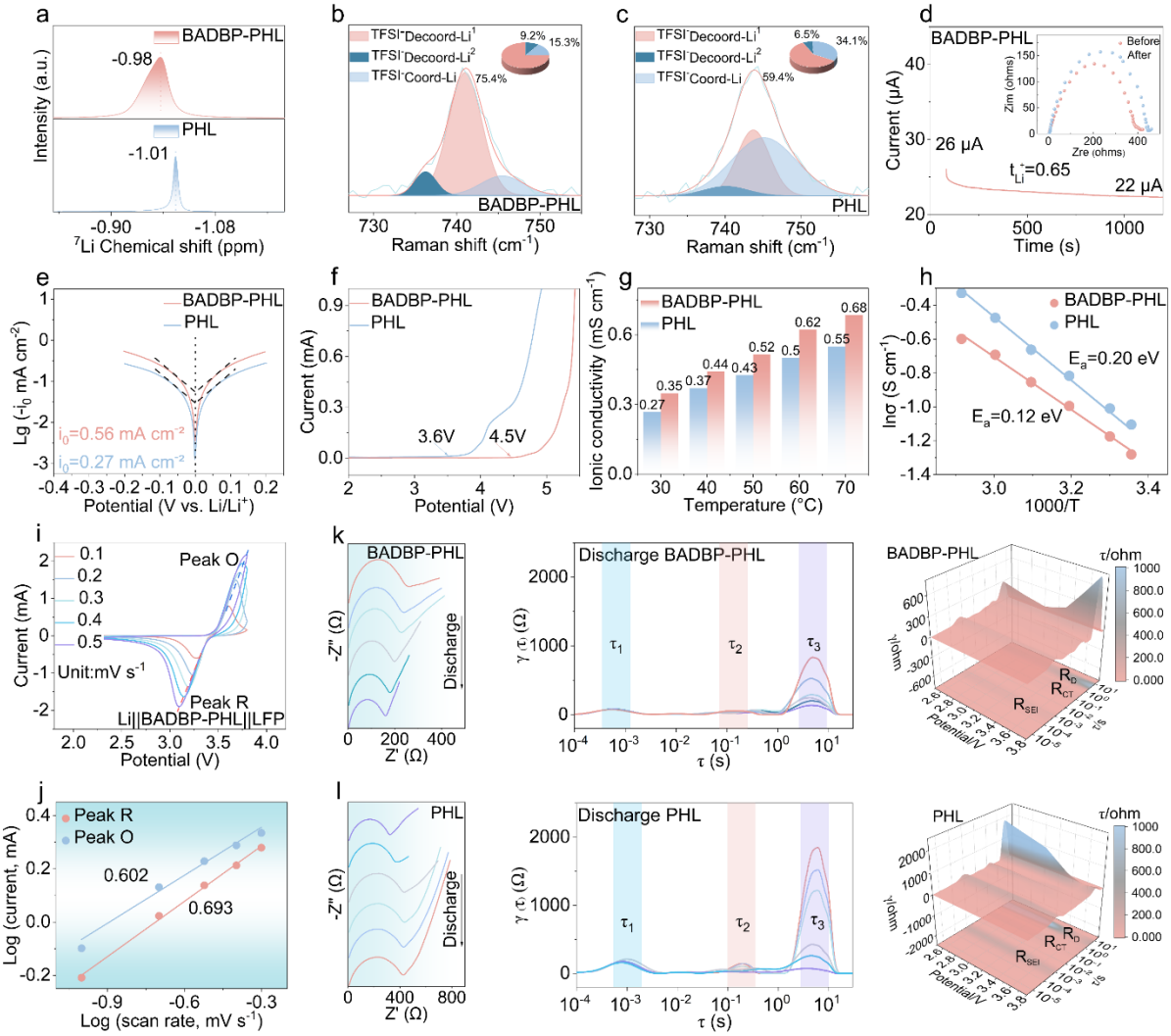

Figure 4. **Spectroscopic and electrochemical characterization of ion transport behavior.** (a) Solid-state ^{7}Li NMR spectra of BADBP-PHL and PHL. Raman spectra of $TFSI^-$ of (b) BADBP-PHL and (c) PHL. (d) Lithium-ion transference number of BADBP-PHL. (e) Tafel curves of PHL and BADBP-PHL. (f) LSV of BADBP-PHL and PHL. (g) Ionic conductivities of BADBP-PHL and PHL at different temperatures. (h) Activation energies of BADBP-PHL and PHL. (i) CV curves and (j) log i and log (scan rate) curves of Li||BADBP-PHL||LFP cell at different scan rates. (k) Resistance curves, DRT change curves, and corresponding 3D mapping diagrams of BADBP-PHL and (l) PHL at 0.5C and discharge at different cycles.

The symmetrical topological structure significantly improves interfacial stability. Cyclic voltammetry (CV) tests of Li||BADBP-PHL||$LiFePO_4$(LFP) cells (Figure 4i) reveal that both the oxidation (0.693) and reduction (0.602) peak currents exhibit logarithmic scan rate slopes greater than 0.5 (Figure 4j), indicating predominantly diffusion-controlled charge storage behavior without significant alteration of the cathode reaction mechanism by BADBP-PHL.[35] Repeated CV cycling at 0.1 mV s^{-1} (Figure S6) demonstrates highly reversible behavior after 5 cycles, confirming exceptional interfacial stability. Further investigation using distribution of relaxation times (DRT) analysis elucidates the interfacial evolution in Li||NCM811 cells (Figures 4k and l). The results show that during charge-discharge cycles (4.3−2.8 V), BADBP-PHL exhibits significantly lower SEI resistance (R_{SEI}, τ_1) compared to PHL, particularly during charging (Figures S7 and S8), suggesting formation of a more stable SEI layer. Concurrently, reduced charge transfer resistance (R_{ct}, τ_2) and diffusion resistance (R_D, τ_3) indicate decreased interfacial energy barriers and accelerated ion transport kinetics.[36–38] These findings collectively demonstrate that the symmetrical topology optimizes interfacial properties, substantially enhancing ionic transport efficiency and conductivity.

Regulation of interfacial stability and lithium deposition behavior

To validate the regulation mechanism of symmetrical molecular topology on lithium-metal interfacial stability, Li||Li symmetric cells with BADBP-PHL electrolyte were systematically evaluated under different rates. As demonstrated in **Figure** 5a, the Li||BADBP-PHL||Li symmetric cell exhibits exceptional cycling stability for 2000 h at 0.1 mA cm^{-2}, maintaining consistently lower overpotential compared to conventional PHL-based cells. Furthermore, as depicted in Figure S9, BADBP-PHL demonstrates remarkable stability for 1000 h even at an elevated current density of 0.5 mA cm^{-2},

whereas the PHL system experiences short-circuit failure after only 250 h of operation with sustained overpotentials exceeding 300 mV. These results unequivocally confirm that the symmetrical molecular topology significantly enhances interfacial stability and effectively suppresses lithium dendrite growth. Notably, BADBP-PHL achieves a superior critical current density (CCD) of 1.3 mA cm^{-2}, substantially higher than PHL's 0.8 mA cm^{-2} (Figure 5b). Rate capability tests (Figure 5c) reveal that BADBP-PHL maintains stable operation across a wide current range of 0.1−1 mA cm^{-2}, in stark contrast to PHL which fails at 0.4 mA cm^{-2}. SEM characterization (Figures 5d and S10) provides compelling evidence that BADBP-PHL enables the formation of significantly thinner (24.61 μm *vs.* 72.73 μm) and more compact lithium deposition layers, conclusively demonstrating that the symmetrical topological structure effectively inhibits dendrite growth through constructing homogeneous ion transport channels.

To elucidate the influence of the symmetrical molecular design on SEI composition and spatial distribution, time-of-flight secondary ion mass spectrometry (TOF-SIMS) depth-profiling analysis was performed on cycled lithium-metal anodes (50 h, Li||Li symmetric cells). The TOF-SIMS analysis reveals distinct compositional differences: the signal intensity of organic components (CH_2^-) in the BADBP-PHL-derived SEI shows significant attenuation (Figures 5e and g), while the signals of LiF_2^- (Figures 5f and h) and $LiBr_2^-$ (Figure S11) exhibit remarkable enhancement. Complementary X-ray photoelectron spectroscopy (XPS) analysis (Figures 5i and j) quantitatively confirms the substantial increase of LiF (685.5 eV) and LiBr (68.9 eV) content in the SEI layer, consistent with the results shown in Figure S12. Notably, the hybrid SEI enriched with inorganic LiF and LiBr components contributes to enhanced stability at the solid electrolyte/anode interface. In particular, the

high Young's modulus and high surface energy of LiF homogenize Li-ion flux, while LiBr exhibits an extremely low diffusion barrier for Li ions.[39,40]

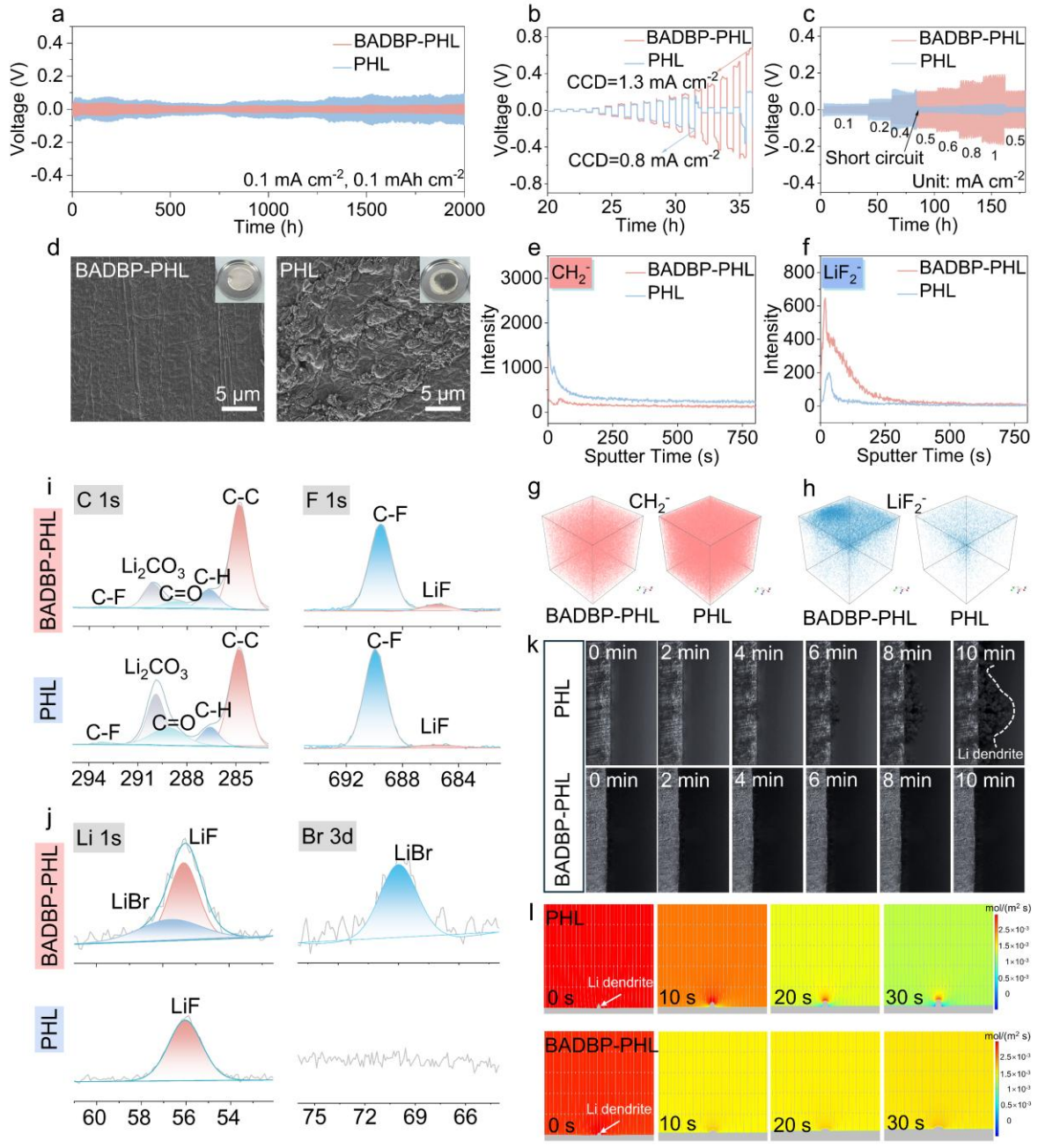

Figure 5. **Interfacial stability and lithium deposition behavior characterizations.** (a) Galvanostatic cycling curves of Li||Li cells using BADBP-PHL and PHL at a current density of 0.1 mA cm^{-2}. (b) CCD of two cells. (c) Rate performance of Li||Li cells. (d) SEM of the lithium metal surface after cycling of two cells. (e) Intensity sputtering distribution of CH_2^- and (f) LiF_2^-, as well as (g) 3D reconstructed distribution of CH_2^- and (h) LiF_2^-. (i) XPS curves of C, F and (j) Li, Br on the lithium metal surface after cycling of BADBP-PHL and PHL-based

cells. (k) In-situ optical microscope images of cross-sections of two cells. (l) COMSOL multiphysics simulation of interfacial lithium growth.

In situ optical microscopy provides direct visual evidence of the deposition dynamics (Figure 5k). At a current density of 0.5 mA cm^{-2}, the PHL system exhibits dendritic nucleation within 4 minutes, progressing to complete mossy coverage by 10 minutes. In striking contrast, BADBP-PHL maintains compact deposition morphology throughout, forming only a uniform, dense thin layer after 10 minutes. Corresponding atomic force microscopy (AFM) measurements (Figure S13) quantitatively confirm the superior surface smoothness of BADBP-PHL deposits (Rq = 29.42 nm). These observations demonstrate the synergistic effect between LiF/LiBr components and the crosslinked network in constructing a homogeneous, stable SEI architecture. Complementary finite element simulation elucidates the dendrite growth behavior (Figure 5l). The PHL system, with its porous defective structure and non-uniform ion transport, facilitates rapid dendritic propagation. During 0-40 s electrodeposition, dendrites preferentially grow along pores before ultimately penetrating the electrolyte membrane. Conversely, BADBP-PHL's crosslinked network eliminates structural defects to form a dense electrolyte layer. This not only establishes uniform ion transport channels (evidenced by minimal temporal variation in Li^+ concentration gradient, Figure S14), but maintains homogeneous current density distribution, thereby effectively suppressing dendrite formation.[41,42] The specific role of BADBP-PHL in stabilizing the lithium anode interface and inhibiting dendrite formation can be categorized into multiple scales: at the molecular level, the formed hybrid SEI enriched with LiF/LiBr contributes to enhanced stability at the solid electrolyte/anode interface; at the mesoscopic scale, the cross-linked network of BADBP-PHL

eliminates voids, optimizes ion channels, and suppresses dendrite growth; macroscopically, it reduces surface roughness and promotes uniform current distribution. These multiscale investigations conclusively demonstrate that the symmetrical topology significantly enhances lithium deposition stability through optimized ion transport homogeneity.

Performance evaluation and safety behaviors of Li metal batteries

Systematic evaluation using Li||NCM811 cells demonstrates the practical advantages of the symmetrical molecular topology. As depicted in **Figures** 6a and S15, the Li||BADBP-PHL||NCM811 cell maintains 82.4% of its capacity after 220 cycles at 0.5C, significantly outperforming the PHL system (60% retention after 157 cycles). This superiority becomes more pronounced under elevated temperatures (Figures 6b, c, and S16). Remarkably, the BADBP-PHL cell achieves 96% capacity retention after 150 cycles at 1 C and 60°C, while the PHL system degrades to 79.1% after only 100 cycles. The universal applicability of this design strategy is further validated in Li||LFP cells (Figures S17 and S18). The exceptional thermal stability originates from the high bond energy of C−Br bonds and the robust three-dimensional crosslinked network within the symmetrical topological structure. Notably, the design exhibits outstanding rate capability, with the Li||BADBP-PHL||LFP cell delivering a reversible capacity of 103.5 mAh g^{-1} at 5 C, representing a significant enhancement compared to the PHL system (87.5 mAh g^{-1}) (Figures 6d and S18).

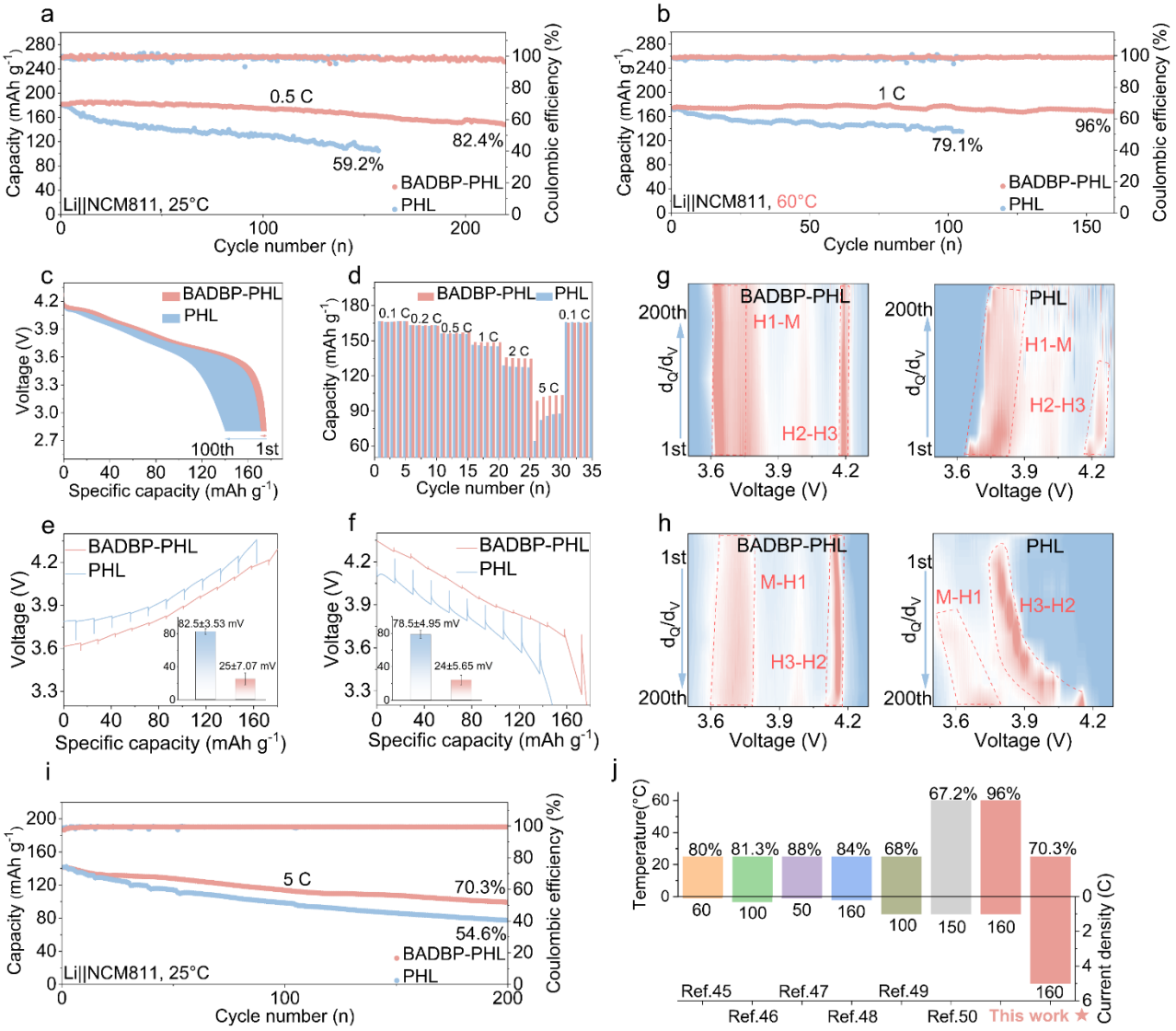

Figure 6. Comprehensive electrochemical performance evaluation of solid-state lithium metal batteries. (a) Cycling performance of Li||BADBP-PHL||NCM811 and Li||PHL||NCM811 cells at 0.5 C and 25°C. (b) Cycling performance and (c) corresponding charge-discharge curves of two cells at 1 C and 60°C. (d) Rate performance of LFP-based batteries. (c) Charge and (f) discharge voltage curves of the cells after 100 cycles measured by GITT. (g) Charge and (h) discharge dQ/dV curves of two cells at different cycles at 0.5 C. (i) Cycling performance of two cells at 5 C and 25°C. (j) Comparison of solid-state Li||NCM811 cells at different temperatures and current densities.

Galvanostatic intermittent titration technique (GITT) characterization uncovers the superior kinetic properties of BADBP-PHL (Figures 6e and f). The BADBP-PHL cell demonstrates higher

specific capacity (>160 mAh g^{-1}) and lower overpotential, primarily due to the enhanced Li^+ diffusion rate and reduced interfacial impedance.[43,44] Differential capacity (dQ/dV) analysis further corroborates the exceptional cycling stability of BADBP-PHL (Figures 6g, h, and S19). Throughout 200 cycles, the Li||BADBP-PHL||NCM811 cell maintains highly consistent redox peak intensities and positions, indicating effective stabilization of the phase transition processes in NCM811 cathodes.[45,46] The fast-charging capability was systematically evaluated at 5C. As shown in Figures 6i and S20, the BADBP-PHL cell retains 70.3% capacity after 200 cycles under these demanding conditions. Comprehensive performance benchmarking reveals that this electrolyte system outperforms most reported solid-state electrolytes across various temperatures and current densities (Figure 6j), unequivocally demonstrating the superiority of the symmetrical molecular topology design.[47–52]

To validate the practical application performance of BADBP-PHL, we comprehensively evaluated all-solid-state pouch cells (**Figure** 7a). Thermal stability tests revealed that under overheating and nail penetration conditions, BADBP-PHL batteries exhibited significantly lower temperature distributions in infrared thermal imaging compared to commercial liquid electrolyte (LE) and PHL systems (Figures 7b and c), confirming superior thermal stability. Notably during nail penetration tests, BADBP-PHL maintained the lowest internal temperature, demonstrating exceptional heat suppression characteristics. Under open flame exposure, BADBP-PHL pouch cells remained non-combustible and explosion-proof (Figure 7d), in stark contrast to the violent combustion observed in LE systems.

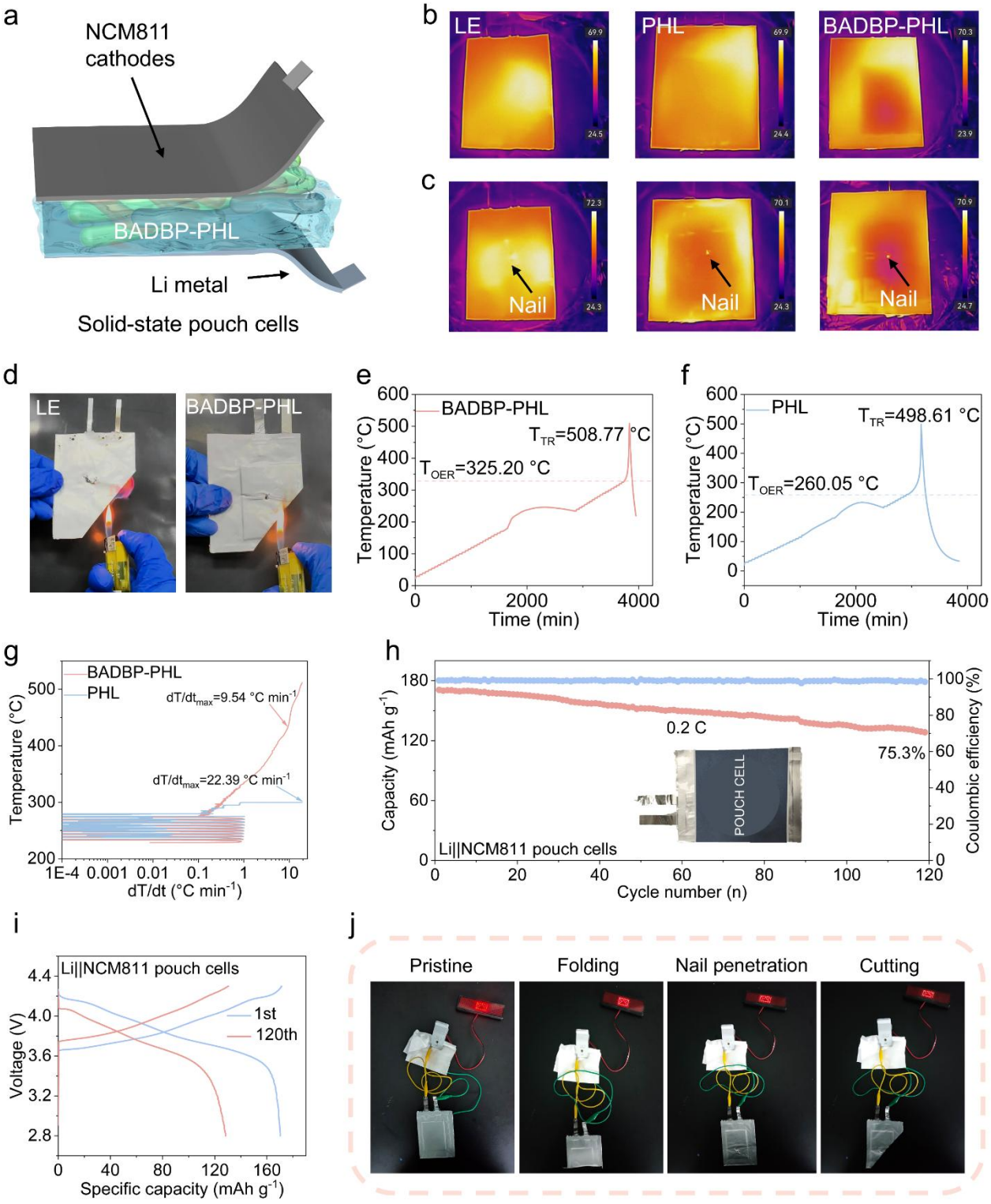

Figure 7. **Safety and electrochemical performance evaluation of pouch cell configurations.** (a) Schematic diagram of Li||NCM811 pouch cell assembled with BADBP-PHL. (b) Infrared thermal images of BADBP and PHL pouch cells under overheating and (c) nail penetration conditions. (d) Combustion experiments of two pouch cells. ARC tests of fully charged (e) BADBP and (f) PHL pouch cells under thermal abuse modes, and

(g) corresponding dT/dt curves *vs.* temperature curves. (h) Cycling performance and (i) the corresponding charge-discharge curves of Li||BADBP-PHL||NCM811 pouch cells. (j) Mechanical abuse validation of Li||BADBP-PHL||NCM811 pouch cells.

The thermal safety of fully charged cells was quantitatively evaluated using accelerated rate calorimetry (ARC) in conjunction with the heat-wait-search (HWS) protocol. By defining the onset temperature of exothermic reaction (T_{OER}, 0.02 °C min^{-1}) and thermal runaway trigger point (T_{TR}, 10 °C min^{-1}), we systematically analyzed thermal runaway behavior. As depicted in Figures 7e and f, BADBP-PHL exhibits a TOER of 325.20 °C, which is higher than PHL (260.05 °C), along with a superior thermal runaway temperature (508.77 °C *vs.* 498.61 °C), demonstrating its ability to suppress exothermic reactions and delay thermal runaway initiation. Notably, BADBP-PHL achieved an exceptionally low maximum temperature rise rate (dT/dt = 9.54°C min^{-1}), underscoring its outstanding thermal stability.[53] These results provide compelling evidence for BADBP-PHL's safety advantages in LMB.

Electrochemical characterization reveals that the Li||BADBP-PHL||NCM811 pouch cell maintains 75.3% capacity retention after 120 cycles (Figure 7h), with highly stable charge/discharge profiles (Figure 7i). More remarkably, the cell demonstrates exceptional mechanical robustness, maintaining normal operation after severe mechanical abuse including folding, perforation, and shearing (Figure 7j). These results conclusively demonstrate that BADBP-PHL not only significantly enhances thermal/mechanical safety in LMB but also preserves outstanding electrochemical performance, showcasing promising potential for practical applications.

Conclusion

This study successfully fabricated an ultrathin 6 μm solid-state polymer electrolyte by integrating the a BADBP symmetric unit into a PH matrix via *in situ* polymerization, forming a robust crosslinked network. The designed electrolyte exhibits three key advantages: Firstly, the symmetric molecular topology of BADBP establishes a three-dimensional crosslinked network, which not only repairs matrix pore defects in the matrix but also significantly reduces crystallinity through the steric hindrance effect of bromophenyl groups. Secondly, the high bond energy of C−Br bonds endows the electrolyte with exceptional thermal stability, while bromine atoms anchor $TFSI^-$ through electrostatic interactions to promote lithium salt dissociation. This optimization yields a room-temperature ionic conductivity of 0.35 mS cm^{-1} coupled with an exceptional Li^+ transference number of 0.65. Furthermore, the *in situ* formed LiF/LiBr-rich SEI layer effectively suppresses dendrite growth, enabling stable cycling of Li||Li cells for 2000 hours at 0.1 mA cm^{-2}. When applied in Li||NCM811 batteries, the electrolyte demonstrates outstanding cycling stability, retaining 82.4% capacity after 230 cycles at room temperature and 96% after 150 cycles at 60°C, along with 5C fast-charging capability. The pouch cells pass rigorous safety tests, including nail penetration and high-temperature exposure, confirming their outstanding practicality and safety. This work provides new insights for developing high-energy-density lithium-metal batteries.

Author Contributions

Kai Chen: Conceptualization, Visualization, Methodology, Writing – original draft. **Anjun Hu:** Investigation, Writing – review & editing. **Wei Yang:** Formal analysis, Supervision, Validation. **Yuanjian Li:** Conceptualization, Visualization. **Zhi Wei Seh:** Formal analysis, Validation. **Fei Li:**

Conceptualization, Visualization. **Jianping Long:** Writing – review & editing, Funding acquisition, Project administration, Supervision. **Shimou Chen:** Writing – review & editing, Validation

Conflicts of Interest

The authors declare no conflict of interest.

Acknowledgements

K.C., A.H., W.Y., and Y.L. contributed equally to this work. A.H. acknowledges the support by Key Laboratory of Sichuan Province for Lithium Resources Comprehensive Utilization and New Lithium Based Materials for Advanced Battery Technology (LRMKF202405), the National Natural Science Foundation of China (52402226), the Sichuan Provincial Natural Science Foundation (2024NSFSC1016), and Chengdu University of Technology's Scientific Research Startup Fund (10912-KYQD2023-10240). Z.W.S. was supported by the Singapore National Research Foundation (NRF Investigatorship NRF-NRFI09-0002) and the Agency for Science, Technology and Research (MTC Programmatic Fund M23L9b0052).

References

[1] H. Liu, Y. Chen, P.-H. Chien, G. Amouzandeh, D. Hou, E. Truong, I. P. Oyekunle, J. Bhagu, S. W. Holder, H. Xiong, P. L. Gor'kov, J. T. Rosenberg, S. C. Grant, Y.-Y. Hu, *Nat. Mater.*, **2025**, *24*, 581–588.

[2] E. P. Alsaç, D. L. Nelson, S. G. Yoon, K. A. Cavallaro, C. Wang, S. E. Sandoval, U. D. Eze, W. J. Jeong, M. T. McDowell, *Chem. Rev.*, **2025**, *125*, 2009–2119.

[3] W. Huang, S. Wang, X. Zhang, Y. Kang, H. Zhang, N. Deng, Y. Liang, H. Pang, *Adv. Mater.*, **2023**, *35*, 2310147.

[4] T. W. Kang, J. Lee, J. Lee, J. H. Park, J. Shin, J. Ju, H. Lee, S. U. Lee, J. Kim, *Adv. Mater.*, **2023**, *35*, 2301308.

[5] T. Li, K. Chen, B. Yang, K. Li, B. Li, M. He, L. Yang, A. Hu, J. Long, *Chem. Sci.*, **2024**, *15*, 12108–12117.

[6] N.-Y. Park, H.-U. Lee, T.-Y. Yu, I.-S. Lee, H. Kim, S.-M. Park, H.-G. Jung, Y.-C. Jung, Y.-K. Sun, *Nat. Energy* **2025**, *10*, 479–489.

[7] Y. M. Jeon, S. Kim, M. Lee, W. B. Lee, J. H. Park, *Adv. Energy Mater.*, **2020**, *10*, 2003114.

[8] S. Zhao, Q. Yua, S. Yang, S. Wan, J. Chen, H. Xu, X. Lou, S. Chen. *Nano Energy*, **2025**, *138*, 110913.

[9] S. Huo, L. Sheng, W. Xue, L. Wang, H. Xu, H. Zhang, X. He, *InfoMat*, **2023**, *5*, e12394.

[10] S. Yang, J. Hu, F. Jiang, H. Yuan, H. S. Park, J. Huang, *InfoMat*, **2024**, *6*, e12512.

[11] H. Liang, M. Zarrabeitia, Z. Chen, S. Jovanovic, S. Merz, J. Granwehr, S. Passerini, D. Bresser, *Adv. Energy Mater.*, **2022**, *12*, 2200013.

[12] H. Liang, L. Wang, A. Wang, Y. Song, Y. Wu, Y. Yang, X. He, *Nano-Micro Lett.*, **2023**, *15*, 42.

[13] S. Duan, L. Qian, Y. Zheng, Y. Zhu, X. Liu, L. Dong, W. Yan, J. Zhang, *Adv. Mater.*, **2024**, *36*, 2314120.

[14] X. Hu, K. Liu, S. Zhang, G. Shao, S. R. P. Silva, P. Zhang, *Nano Res.*, **2024**, *17*, 2790–2799.

[15] T. Deng, L. Cao, X. He, A.-M. Li, D. Li, J. Xu, S. Liu, P. Bai, T. Jin, L. Ma, M. A. Schroeder, X. Fan, C. Wang, *Chem*, **2021**, *7*, 3052–3068.

[16] S. Liu, L. Zhou, T. Zhong, X. Wu, K. Neyts, *Adv. Energy Mater.*, **2024**, *14*, 2403602.

[17] X. Pang, B. Shi, Y. Liu, Y. Li, Y. Zhang, T. Wang, S. Xu, X. Wang, Z. Liu, N. Xing, X. Liang, Z. Zhu, C. Fan, Y. Liu, H. Wu, Z. Jiang, *Adv. Mater.*, **2024**, *36*, 2413022.

[18] K. Yang, L. Chen, J. Ma, C. Lai, Y. Huang, J. Mi, J. Biao, D. Zhang, P. Shi, H. Xia, G. Zhong, F. Kang, Y. He, *Angew. Chem. Int. Ed.*, **2021**, *60*, 24668–24675.

[19] D. Luo, M. Li, Q. Ma, G. Wen, H. Dou, B. Ren, Y. Liu, X. Wang, L. Shui, Z. Chen, *Chem. Soc. Rev.*, **2022**, *51*, 2917–2938.

[20] S. Zhao, Y. Shen, H. Che, M. Jabeen, C. Lu, X. Liao, Z. Ma, *Adv. Funct. Mater.*, **2024**, *35*, 2422162.

[21] F. Li, T. Dong, Y. Ji, L. Liang, K. Chen, H. Zhang, G. Cui, G. Hou, *J. Energy Chem.*, **2024**, *93*, 377–383.

[22] N. Ding, S. W. Chien, T. L. D. Tam, X. Li, G. Wu, W. J. Lee, S. Y. Chiam, Y. S. Meng, D. W. H. Fam, *Adv. Energy Mater.*, **2024**, *14*, 2402986.

[23] M. Zhang, H. Wang, A. Shao, Z. Wang, X. Tang, S. Li, J. Liu, Y. Ma, *Adv. Energy Mater.* **2024**, *14*, 2303932.

[24] M. Bai, X. Tang, M. Zhang, H. Wang, Z. Wang, A. Shao, Y. Ma, *Nat. Commun.* **2024,** *15*, 5375.

[25] Y. Wu, Z. Tian, B. Li, J. Gu, H. Yuan, W. Liu and H. Ge, *J. Hazard. Mater.*, **2024**, *465*, 132943.

[26] Q. Sun, S. Wang, Y. Ma, D. Song, H. Zhang, X. Shi, N. Zhang, L. Zhang, *Adv. Mater.*, **2023**, *35*, 2300998.

[27] M. Ding, R. Shi, J. Qu, M. Tong, *Chin. Chem. Lett.*, **2023**, *34*, 108248.

[28] B. Yang, Y. Pan, T. Li, A. Hu, K. Li, B. Li, L. Yang, J. Long, *Energy Storage Mater.*, **2024**, *65*, 103124.

[29] J. Chen, A. Hu, K. Chen, Y. Xia, W. Xu, K. Li, B. Yang, T. Li, R. Xu, Z. Wang, B. Li, F. Li, J. Long, *Nano Energy*, **2025**, *139*, 110959.

[30] Y. Wang, H. Tu, A. Sun, L. Wang, F. Zhu, P. Xue, J. Wang, F. Ye, M. Liu, *Chem. Eng. J.*, **2023**, *475*, 146414.

[31] Y. Ye, X. Zhu, N. Meng, F. Lian, *Adv. Funct. Mater.*, **2023**, *33*, 2307045.

[32] G. Feng, Q. Ma, D. Luo, T. Yang, Y. Nie, Z. Zheng, L. Yang, S. Li, Q. Li, M. Jin, X. Wang, Z. Chen, *Angew. Chem. Int. Ed.*, **2025**, *64*, e202413306.

[33] X. Qi, Y. Li, S. Zhang, X. Li, X. Wang, H. Jiang, X. Wu, X. Ruan, X. Jiang, G. He, J. Tu, *Chem. Eng. J.*, **2024**, *501*, 157701.

[34] D. Zhang, Y. Liu, Z. Sun, Z. Liu, X. Xu, L. Xi, S. Ji, M. Zhu, J. Liu, *Angew. Chem. Int. Ed.*, **2023**, *62*, e202310006.

[35] P. Wang, Y. Liu, J. Cui, L. Zhao, D. Li, Y. Du, H. Li, *Adv. Funct. Mater.*, **2024**, *35*, 2414430.

[36] R. Xu, A. Hu, Z. Wang, K. Chen, J. Chen, W. Xu, G. Wu, F. Li, J. Wang, J. Long, *J. Energy Chem.*, **2025**, *105*, 35–43.

[37] S. Lei, Z. Zeng, Y. Wu, M. Liu, S. Cheng and J. Xie, *Chem. Eng. J.*, **2023**, *463*, 142181.

[38] M. He, Y. Fan, S. Liu, S. Wang, T. Wu, D. Chen, A. Hu, C. Yan, Y. Yan, J. Long, Y. Hu, T. Lei, P. Li, W. Chen, *Adv. Energy Mater.*, **2025**, *15*, 2405642.

[39] S. Yan, F. Liu, Y. Ou, H. Zhou, Y. Lu, W. Hou, Q. Cao, H. Liu, P. Zhou, K. Liu, *ACS Nano* **2023**, *17, 19,* 19398–19409.

[40] K. Vishweswariah, N. G. Ningappa, M. D. Bouguern, A. Kumar M R, M. B. Armand, K. Zaghib, *Adv. Energy Mater.* **2025**, 2501883.

[41] Z. Han, R. Zhang, J. Jiang, Z. Chen, Y. Ni, W. Xie, J. Xu, Z. Zhou, J. Chen, P. Cheng, W. Shi, *J. Am. Chem. Soc.*, **2023**, *145*, 10149–10158.

[42] S. Luo, Z. Wang, X. Li, X. Liu, H. Wang, W. Ma, L. Zhang, L. Zhu, X. Zhang, *Nat. Commun.*, **2021**, *12*, 6968.

[43] C. Zhu, C. Sun, R. Li, S. Weng, L. Fan, X. Wang, L. Chen, M. Noked, X. Fan, *ACS Energy Lett.*, **2022**, *7*, 1338–1347.

[44] W. Xue, M. Huang, Y. Li, Y. G. Zhu, R. Gao, X. Xiao, W. Zhang, S. Li, G. Xu, Y. Yu, P. Li, J. Lopez, D. Yu, Y. Dong, W. Fan, Z. Shi, R. Xiong, C.-J. Sun, I. Hwang, W.-K. Lee, Y. Shao-Horn, J. A. Johnson and J. Li, *Nat. Energy*, **2021**, *6*, 495–505.

[45] H. Ji, J. Wang, H. Qu, J. Li, W. Ji, X. Qiu, Y. Zhu, H. Ren, R. Shi, G. Ji, W. Zhao and G. Zhou, *Adv. Mater.*, **2024**, *36*, 2407029.

[46] X. Wu, Z. Piao, M. Zhang, G. Lu, C. Li, K. Jia, Z. Zhuang, R. Gao and G. Zhou, *J. Am. Chem. Soc.*, **2024**, *146*, 14036–14047.

[47] C. Zhao, Q. Zhao, X. Liu, J. Zheng, S. Stalin, Q. Zhang, L. Archer, H., *Adv. Mater.* **2020**, *32*, 1905629.

[48] S. Zhang, F. Sun, X. Du, S. Pan, X. Zhang, L. Huang, J. Ma, S. Dong, A. Hilger, I. Manke, L. Li, B. Xie, J. Li, Z. Hu, A. Komarek, H. Lin, C. Kuo, C. Chen, P. Han, G. Xu, Z. Cui and G. Cui, *Energy Environ. Sci.,* **2023**, *16*, 2591.

[49] Y.-F. Huang, T. Gu, G. Rui, P. Shi, W. Fu, L. Chen, X. Liu, J. Zeng, B. Kang, Z. Yan, F. J. Stadler, L. Zhu, F. Kang and Y.-B. He, *Energy Environ. Sci.*, **2021**, *14*, 6021–6029.

[50] S. Xia, B. Yang, H. Zhang, J. Yang, W. Liu and S. Zheng, *Adv. Funct. Mater.*, **2021**, *31*, 2101168.

[51] J. Pan, Y. Zhang, J. Wang, Z. Bai, R. Cao, N. Wang, S. Dou and F. Huang, *Adv. Mater.* **2022**, *34*, 2107183.

[52] K. Yang, L. Chen, J. Ma, C. Lai, Y. Huang, J. Mi, J. Biao, D. Zhang, P. Shi, H. Xia, G. Zhong, F. Kang and Y. He, *Angew. Chem. Int. Ed.*, **2021**, *60*, 24668–24675.

[53] K. Chen, A. Hu, G. Zhu, Y. Li, J. Jiang, B. Yang, T. Li, K. Li, J. Chen, W. Xu, Z. Wang, R. Xu, W. Yang, J. Wang, G. Wu, J. Long, and Z. Seh. *ACS Nano*, **2025**, *19*, 14284−14298.